Chapter 8
Ozone Added Spark Assisted Compression Ignition

Sayan Biswas and Isaac Ekoto

Abstract The mixed-mode engine combustion strategy where some combination of spark-assisted compression ignition (SACI) and pure advanced compression ignition (ACI) are used at part-load operation with exclusive spark-ignited (SI) combustion used for high power-density conditions has the potential to increase efficiency and decrease pollutant emissions. However, controlling combustion and switching between different modes of mixed-mode operation is inherently challenging. This chapter proposes to use ozone (O_3)—a powerful oxidizing chemical agent—to maintain stable and knock-free combustion across the load-speed map. The impact of 0–50 ppm intake seeded O_3 on performance, and emissions characteristics was explored in a single-cylinder, optically accessible, research engine operated under lean SACI conditions with two different in-cylinder conditions, (1) partially stratified (double injection—early and late injection) and (2) homogeneous (single early injection). O_3 addition promotes end gas auto-ignition by enhancing the gasoline reactivity, which thereby enabled stable auto-ignition with less initial charge heating. Hence O_3 addition could stabilize engine combustion relative to similar conditions without O_3. The addition of ozone has been found to reduce specific fuel consumption by up to 9%, with an overall improvement in the combustion stability compared to similar conditions without O_3. For the lowest loads, the effect of adding O_3 was most substantial. Specific NO_x emissions also dropped by up to 30% because a higher fraction of the fuel burned was due to auto-ignition of the end gas. Measurement of in-cylinder O_3 concentrations using UV light absorption technique showed that rapid decomposition of O_3 into molecular (O_2) and atomic oxygen (O) concurred with the onset of low-temperature heat release (LTHR). The newly formed O from O_3 decomposition initiated fuel hydrogen abstraction reactions responsible for early onset of LTHR. At the beginning of high-temperature heat release (HTHR), end gas temperatures ranged from 840 to 900 K, which is about 200 K cooler than those found in previous studies where intake charge heating or extensive retained residuals were used to preheat the charge. An included analysis indicates that in order to achieve optimal auto-ignition in our engine, the spark deflagration was needed to add

S. Biswas (✉) · I. Ekoto
Sandia National Laboratories, Livermore, CA 94550, USA
e-mail: sayanbiswas@ieee.org

A. P. Singh et al. (eds.), *Advanced Combustion Techniques and Engine Technologies for the Automotive Sector*, Energy, Environment, and Sustainability,
https://doi.org/10.1007/978-981-15-0368-9_8

10–40 J of additional thermal energy to the end gas. We have leveraged these results to broaden our understanding of O_3 addition to different load-speed conditions that we believe can facilitate multiple modes (SI, ACI, SACI, etc.) of combustion.

Keywords O_3 addition · Spark assisted compression ignition (SACI) · Low-temperature heat release (LTHR) · Homogeneous versus stratified combustion · Advanced plasma ignition

Definitions/Abbreviations

ϕ	Equivalence ratio
σ_{O_3}	Ozone absorption cross-section
ACI	Advanced compression ignition
AHRR	Apparent heat release rate
B	Bore diameter
BDI	Barrier discharge igniter
CA	Crank angle referenced to main TDC
CA50	50% cumulative burn angle
CO	Carbon monoxide
CO_2	Carbon dioxide
CoV	Coefficient of variation
C_p	Constant pressure specific heat
DI	Direct injection
E	Energy
EGR	Exhaust gas recirculation
EI	Emission index
EVC/EVO	Exhaust valve close/open
DI	Direct injection
GCI	Gasoline compression ignition
H/C	Hydrogen-to-carbon ratio
H_2O	Water
HO_2	Hydroperoxyl
H_2O_2	Hydrogen peroxide
HC	Hydrocarbon
HTHR	High-temperature heat release
I_{ref}	Reference intensity
IMEP	Indicated mean effective pressure
ISFC	Indicated specific fuel consumption
ITE	Indicated thermal efficiency
ITHR	Intermediate-temperature heat release
IVC/IVO	Intake valve close/open
LHV	Lower heating value
LTC	Low-temperature combustion

LTHR	Low-temperature heat release
LTP	Low-temperature plasma
m	Mass
MBT	Maximum brake torque
N_2	Nitrogen
NO	Nitric oxide
NO_2	Nitrogen dioxide
NO_x	Nitrogen oxide
NVO	Negative valve overlap
O	Atomic oxygen
O_2	Molecular oxygen
O_3	Ozone
OH	Hydroxyl
OS	Octane sensitivity
P	Pressure
PID	Proportional, Integral, Derivative
PM	Particulate matter
PMT	Photomultiplier tube
ppm	Parts per million
PVO	Positive valve overlap
R	Alkyl radical
R	Gas constant
RGF	Residual gas fraction
RI	Ringing intensity
ROOH	Alkylhydroperoxide
RON	Research octane number
rpm	Revolutions per minute
SACI	Spark assisted compression ignition
SI	Spark ignition
SOI	Start of injection
ST	Spark timing
T	Temperature
T10/T50/T90	10, 50, and 90% boiling points
TDC	Top dead center
TPI	Transient plasma ignition
UHC	Unburned hydrocarbon
UV	Ultraviolet

Subscripts

1, **2**	First injection, second injection
b	Burned
bulk	Bulk/Averaged

exh	Exhaust
f	Fuel
int	Intake
r	Residual
ref	Reference
u	Unburned

8.1 Introduction

Conventional compression-ignition (CI) engines provide a plausible solution to light-duty vehicle manufacturers due to their improved efficiency operating at higher compression ratio compared to spark-ignition (SI) gasoline engines (Dec 2009). However, controlling the emissions of nitrogen oxide (NO_x) and particulate matter (PM) are the biggest challenges for CI engines (Stone 1999; Biswas 2018). As emission standards continue to become stricter, future engine control strategies will be a combination of combustion optimization, fuel refinement, and aggressive exhaust after-treatment technologies—all of which add significant cost and complexity to the engine architecture (United States, Environmental Protection Agency, Office of Transportation and Air Quality 2012; Graham et al. 2009; United States Environmental Protection Agency, Office of Policy and Evaluation 2016; Biswas et al. 2016; Biswas and Qiao 2016). On the other hand, even though homogeneous charge compression ignition (HCCI) combustion offers high thermal efficiency and ultra-low NO_x and PM emissions (Stanglmaier and Roberts 1999; Christensen et al. 1997; Weinrotter et al. 2005; Srivastava et al. 2009), it is limited by a lack of a direct control mechanism for ignition timing and combustion phasing (Zhao et al. 2003). One way to address this control issue is to explore mixing controlled advanced compression ignition (ACI) strategies such as gasoline compression injection (GCI), and spark-assisted compression ignition (SACI) that use some amount of bulk-gas auto-ignition of gasoline-like fuels. Within controlled laboratory environments, mixing controlled ACI strategies have demonstrated the efficiency benefits of CI and the low engine-out emissions of SI (Saxena and Bedoya 2013).

The main challenge for ACI approaches is to keep stable and knock-free operation throughout the entire load-speed map. Poor combustion stability at low load conditions can be improved by tailoring the charge reactivity through some combination of injection strategy, intake heating, excessive usage of retained residual, charge motion, and piston bowl design (Fitzgerald and Steeper 2010; Kolodziej et al. 2015; Wolk et al. 2016a, b). These solutions for improved stability come at the cost of increased heat transfer losses (Ekoto et al. 2017) and more complex valve train requirements. For high load conditions, heavy use of exhaust gas recirculation (EGR) is required to slow heat release rates (Dec et al. 2015; Dernotte et al. 2015) and to reduce engine knock propensity, which then requires heavy intake boosting to meet load demands. Consequently, expansion efficiency is reduced, and mechanical losses are increased due to the higher peak cylinder pressure requirements. Each of these alternatives contributes to the price and complexity that should have been avoided by using ACI.

A practical near-term alternative to ACI engine combustion is the so-called dual- or mixed-mode combustion strategy, where the idea is to run the engine in SI mode for high power-density conditions (Lawler and Filipi 2013; Manofsky et al. 2011) and in SACI mode at low and part load to keep up efficiency. The SACI strategy differs from conventional SI engines in that elevated unburned gas temperatures induced by compression heating from an expanding spark initiated flame kernel (Persson et al. 2007; Reuss et al. 2008; Lavoie et al. 2010; Benajes et al. 2013, 2014; Olesky et al. 2013, 2014, 2015; Ortiz-Soto et al. 2014; Middleton et al. 2015) are utilized to promote end gas auto-ignition. Moderate to high EGR dilution is used to limit adiabatic flame temperatures and heat release rates. Turbo- and super-charging can recover part of the power density losses due to EGR dilution at high load results peak cylinder pressures very near to knocking conditions. Although SACI benefits from higher compression ratios, high-power-density SI conditions dictate that compression ratios should be set to below 14 to avoid knock. This is significantly below 16+ compression ratios commonly employed for conventional ACI. Therefore, some combination of mixture stratification and charge heating becomes unavoidable to ensure enhanced gasoline reactivity sufficient for end gas auto-ignition.

However, charge reactivity can be increased by seeding a small amount (less than 50 ppm) of Ozone (O_3)—a powerful oxidizing chemical agent to the intake charge. Compared to other additives, O_3 is a particularly promising candidate that can be generated onboard via increasingly inexpensive and compact O_3 generators or even by low-temperature plasma discharges from advanced ignition systems (Uddi et al. 2009). Thus, O_3 addition enables stable auto-ignition with lower intake heating or complex valve train adjustments (Masurier et al. 2013, 2015a, b; Truedsson et al. 2017; Pinazzi and Foucher 2017; Ekoto and Foucher 2018). The idea of adding O_3 to improve fuel reactivity is not new (Ombrello et al. 2010; Zhang et al. 2016). Masurier et al. (2015b) compared various oxidizing species such as nitric oxide, nitrogen oxide, and O_3 affecting engine performance and O_3 found to be the most effective additive among them. Truedsson et al. (2017) demonstrated that O_3 addition could facilitate ignition of high octane rating fuels blended with ethanol that are otherwise difficult to ignite in HCCI combustion.

Ozone-assisted oxidation—'ozonolysis,' has lately drawn considerable interest in low-temperature combustion research due to the increase of plasma-assisted combustion methods and chemically controlled engine designs. Rousso et al. (2018) studied ethylene oxidation in a jet-stirred reactor and observed ozonolysis below 600 K. However, the O_3 decomposition rate increases rapidly above 600 K. Above 600 K temperature, O_3 rapidly decomposes into molecular and atomic oxygen (O) (Masurier et al. 2013; Depcik et al. 2014). The O radical then initiates heat release through fuel hydrogen (H) abstraction reaction to form alkyl (R) and hydroxyl (OH) radicals (Ekoto and Foucher 2018; Smekhov et al. 2007). The OH radical further reacts with fuel and continues the H abstraction reaction. This initiates low-temperature heat release (LTHR) pathways that occurs at temperatures below ~800 K. Furthermore, R combining with molecular oxygen (O_2) forms peroxy radicals (RO_2). Then RO_2 participates in ongoing fuel H abstraction reaction through $RO_2 + RH \rightarrow ROOH + R$. The breakdown of alkyl hydroperoxide (ROOH) into alkyloxy radical (RO) and OH then becomes a sustainable source of LTHR radicals (Zádor et al. 2011). These early LTHR reactions can progress combustion phasing by more than 20 crank angles (CA) depending on the initial O_3 concentrations.

In this chapter, the effect of intake seeded O_3 was investigated as a way to replace charge pre-heating for stable lean SACI operation with two different injection strategies, (1) Partially stratified: double injection—early (75–90% fuel) and late DI (10–25% fuel), and (2) Homogeneous: single early direct injection (DI). Experiments have been carried out in an optically accessible single-cylinder spray-guided research engine. For the partially stratified double injection strategy, O_3 concentrations required to achieve stable combustion were lower at between 30 and 34 ppm. Low to moderate engine loads of between 1.5 and 5.5 bar IMEP and speeds of between 800 and 1600 rpm were examined. For all single injection homogeneous conditions, moderate engine loads of between 4 and 5 bar indicated mean effective pressure (IMEP) and speeds of between 800 and 1400 revolution per minute (rpm) were examined. O_3 concentrations were set at 50 ppm—the peak attainable concentration at the highest 1400 rpm engine speed assessed with the current O_3 generator. Note that the O_3 concentration was reduced from 50 to 31 ppm for a single low speed and high intake temperature due to excessive knocking with higher O_3 concentration. For both fueling strategies, a naturally aspired intake pressure was maintained, with internal residual gas fractions (RGF) between 10 and 20% achieved by combining positive valve overlap (PVO) with moderate exhaust backpressures. For the homogeneous strategy intake temperatures were swept between 42 and 80 °C, while for partially stratified strategy a constant 42 °C intake temperature was maintained for all conditions. Each load/speed operating condition was optimized to maximize engine performance while maintaining NO_x emissions and ringing intensity (RI) below 5 g/kg-fuel and 1 MW/m^2 respectively. Performance and engine-out emissions measurements were complemented by CA resolved O_3 measurements performed via ultraviolet (UV) light absorption and single-zone chemical kinetic modeling of end gas LTHR.

8.2 Experimental Methods

8.2.1 Sandia Single-Cylinder Research Engine

All engine testing was conducted in a single-cylinder engine that featured a Bowditch piston, four-valve pent-roof, spray-guided injection, and optical access as shown schematically in Fig. 8.1. The optical access into the engine cylinder was provided via diametrically opposed wall-mounted quartz windows (12.7 mm aperture). Research-grade RD587 gasoline was directly injected into the cylinder via a centrally located

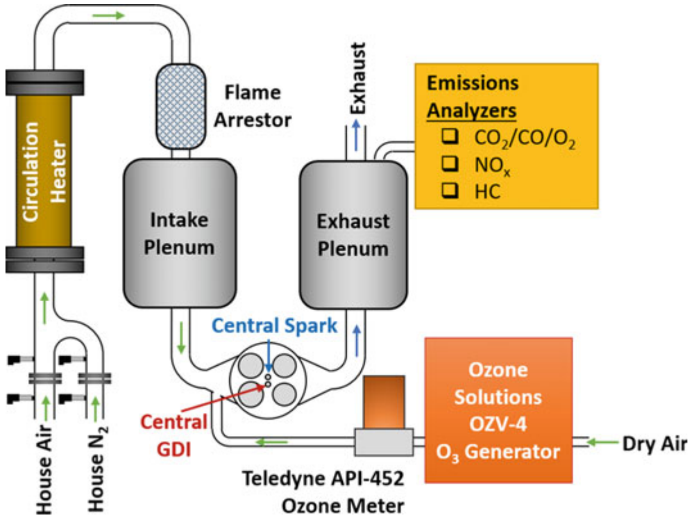

Fig. 8.1 Schematic of the Sandia light-duty optical gasoline engine, gas supply system, O_3 generator, and emissions measurement setup

Bosch HDEV1.2 injector with eight uniformly distributed 125 μm diameter nozzles forming a 60° umbrella angle. The ignition system consisted of a long-reach resistor type spark plug (NGK 12 mm nominal thread), and a Bosch 93 mJ ignition coil. Intake and exhaust cams were set to create a positive valve overlap (PVO) of 34 crank angles at TDC. An engine dynamometer was used to vary engine speeds. An optical encoder (BEI sensors) with 0.1 CA resolution was used to locate the crank angle position. Intake port and runner designs are optimized to limit swirl and tumble flows to reduce heat transfer losses via in-cylinder turbulence. An Aquatherm heat exchanger was used to maintain a constant cylinder wall temperature to 90 °C.

A Tescom ER5000 PID (Proportional, Integral, Derivative) pneumatic actuator was used to precisely regulate the intake air supply. In both the intake and exhaust runners, pressure and temperature were measured. The exhaust runner was heated using wire-wrapped resistive heaters and fiberglass insulation to minimize the heat transfer losses. A Chromalox circulation heater located between the intake plenum and air supply was used to heat the intake charge up to 80 °C. A piezoelectric pressure sensor (Kistler 6125A) was used to measure cylinder pressure history. Heat release and load in every cycle were estimated from the in-cylinder pressure trace.

A two-zone pressure-based heat release assessment was conducted where the cylinder volume was divided into burned and unburned regimes so that unburned temperatures could be estimated at the onset of end gas LTHR and HTHR. The onset of LTHR was estimated from apparent heat release rate (AHRR) profile difference with and without O_3 addition operating at the identical conditions. In the burned gas region, the two-zone model presumed complete combustion of the fuel. The burned gas temperature was calculated from the heat of combustion of the consumed fuel.

Since major portion of heat release was from the end gas auto-ignition, a modified Woschni correlation for ACI combustion (Chang et al. 2004) served best to estimate the heat loss.

Ozone generated by an external O_3 generator (Ozone Solutions OZV-4) directly seeded into the intake runner. The O_3 concentration was varied by changing the amount of dry air using a mass flow controller (MKS GE50) passing through the O_3 generator. An O_3 meter (Teledyne API 452) was used to monitor the O_3 concentration out of the O_3 generator. Table 8.1 summarizes significant details on engine geometry, valve timings, and operating conditions, and fueling strategies.

For all experiments, research-grade RD587 gasoline with a RON of 92.1 and octane sensitivity of 7.3 was used. Table 8.2 summarizes the essential physical and chemical properties of RD587.

Pollutant emissions from the exhaust plenum were sampled for fired cycles using heated sampling lines to minimize condensation of water and fuel. A CAI 600

Table 8.1 Engine specifications and operating conditions

Engine specifications		
Displaced volume (L)	0.551	
Bore/stroke/connecting rod (mm)	86/95.1/166.7	
Geometric compression ratio	13:1	
Intake valve open/close (CA)[a]	343/−145	
Exhaust valve open/close (CA)[a]	160/−343	
Valve lift (mm)	9.7	
Fuel pressure (bar)	100	
Injector hole number	8	
Injector cone angle (°)	60	
Injector orifice diameter (μm)	125	
Operating conditions		
	Partially stratified	Homogeneous
Intake/exhaust pressure (kPa)	100/105	100/110
Intake temperature (°C)	42	42–80
Intake O_3 concentration (ppm)	0–34	0–50
Engine speed (rpm)	800, 1000, 1200, 1400, 1600	800, 1000, 1200, 1400
Cycle fueling rates (mg/cycle)	8.1–17.9	13.4–16.9
Equivalence ratio	0.27–0.56	0.37–0.45
RGF (%)	10–18	12–20
Spark timing (CA)	−70 to −28	−60 to −55
Main start of injection (SOI) (CA)[a]	−230	−330
2nd injection SOI (CA)	−64 to −36	–
2nd injection fueling fraction (%)	10–25	0

[a]0 CA corresponds to TDC of the compression stroke

Table 8.2 Physical and chemical properties of RD587 gasoline

Liquid density @ 15 °C (g/L)	748
LHV (kJ/mg)	41.9
H/C ratio	1.972
O/C ratio	0.033
Research octane number	92.1
Octane sensitivity	7.3
T10/T50/T90 (°C)	57/98/156

NDIR/Oxygen Multi-Component analyzer was used to measure the dry engine out emission of carbon monoxide (CO), carbon dioxide (CO_2), and oxygen (O_2). A CAI 600 HFID was employed to measure hydrocarbon (HC) emissions. Measurements of CO and HC measurements were used in conjunction along with measured airflow and fuel injection rates to estimate combustion efficiency. A CAI 600 HCLD NO/NO_x chemiluminescence analyzer was used to measure oxides of Nitrogen (NO_x).

8.2.2 Partially Stratified Versus Homogeneous SACI

Figure 8.2 illustrates the injection strategies along with the in-cylinder combustion processes for partially stratified and homogeneous conditions. For partially stratified SACI, each cycle featured an early direct injection with a fixed SOI at −230 CA and a late second injection with the SOI timed just after ST. The second injection SOI was varied between −64 and −36 CA. While a greater quantity of fuel 75–90%

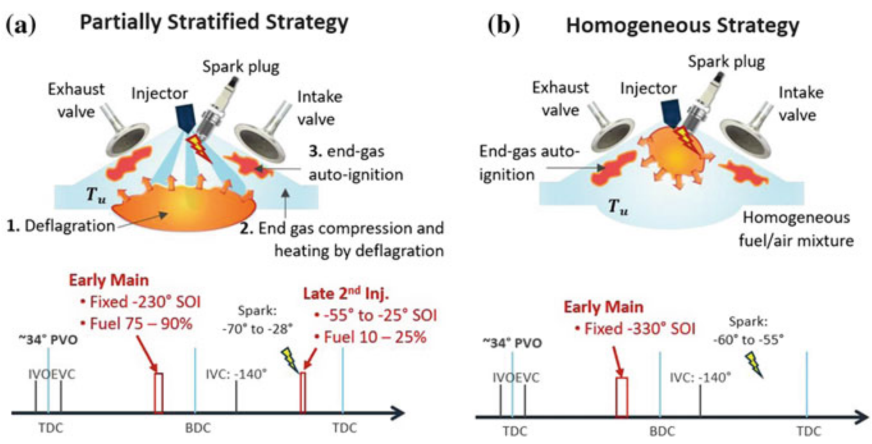

Fig. 8.2 Schematic of in-cylinder combustion processes and cycle events for **a** partially stratified, **b** homogeneous SACI

was injected in the early cycle, a small quantity of late-cycle injection 10–25% helped stabilize the combustion. Two of the fuel sprays straddle the spark plug gap with virtually all of the fuel spray for injections later than −80 CA entering the piston bowl. The initial deflagration is believed to be confined to the piston bowl where mixtures are fuel-rich. Compressive heating by the deflagration then leads the leaner end gas mixtures to transition to auto-ignition. To find the optimum operating points for partially stratified SACI, ST and second injection timing/quantity were adjusted for each operating point until MBT conditions were reached provided that ringing intensity values and engine-out NO_x emissions remained below 1 MW/m^2 and 5 g/kg-fuel respectively.

For homogeneous SACI, an early DI with SOI set at −330 CA created a homogeneous charge in the cylinder. The initial deflagration created by the spark ignition propagated into the cylinder and led to an end gas auto-ignition. The intake seeded 50 ppm O_3 along with the moderate RGF of between 12 and 20% tailored the end gas reactive enough to auto-ignite. However, slight intake heating 42–80 °C was necessary to stabilize combustion. The engine speed was a key factor that affected the O_3 decomposition and end gas auto-ignition behavior. To locate the optimum operating conditions for homogeneous SACI, the fueling rate at maximum brake torque (MBT) spark timing (ST) was adjusted until the minimum achievable load was met, provided that the coefficient of variation (CoV) of IMEP was below 3%, the ringing intensity (RI) was below 1 MW/m^2, and NO_x emissions were below 1 g/kg-fuel.

The intake seeded O_3 concentration (30–34 ppm) for partially stratified SACI was lower than that was required for homogeneous SACI. Note that intake temperature was fixed at 42 °C in partially stratified SACI. Similar to the homogenous SACI, an exhaust pressure of 1.05 bar in conjunction with the use of PVO produced moderate RGF of between 10 and 18%. The engine was motored for approximately 30 s for each experiment with the O_3 generator switched on to accumulate uniform and constant O_3 levels in the intake runner. Using a predefined spark timing, the engine was then fired for about 90 s. The injection quantity and ST were adjusted gradually to the desired set point after the 90-s warm-up period. Once combustion and engine-out emissions readings become steady, a 100-cycle dataset was collected for every operating point. Before the engine was stopped to oil the rings, O_3 generator was switched off and the engine was motored to clear out residual emission in the exhaust runner. This entire process was repeated for the next experimental condition.

8.2.3 In-Cylinder O_3 Measurement

The in-cylinder-averaged O_3 concentrations were estimated using UV light absorption on a CA basis, as shown in Fig. 8.3. This in-cylinder O_3 measurement technique has been discussed in detail in our earlier work (Biswas and Ekoto 2019a, b). Hence a brief description is presented here for the readers' convenience. Partly collimated 250-Watt continuous broadband light generated from a Xenon arc lamp (Spectra physics 66924-250XV) was transmitted through the optical engine into an integrating

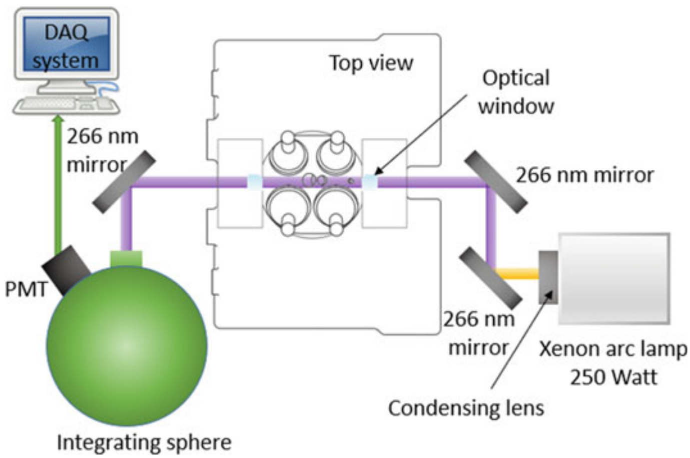

Fig. 8.3 Schematic representation of the O_3 absorption diagnostic

sphere followed by a photomultiplier tube (PMT, Pacific Instruments 3150RF) using several Nd: YAG 4th harmonic laser line mirrors that reflected only the 266 nm light. The absorption cross-section of O_3 (σ_{O_3}) at 266 nm is 9.37×10^{-18} cm^2/molecule (Gorshelev et al. 2014). The optical setup is shown in Fig. 8.3 minimized beam steering effect attributed to the thermal gradients within the combustion chamber. Finally, the Beer-Lambert law was used to calculate the CA resolved O_3 mole fraction, X_{O_3}.

$$X_{O_3} = \frac{k_B T_{bulk}}{p B \sigma_{O_3}} \ln \frac{\mathbb{I}_{ref}}{\mathbb{I}} \tag{8.1}$$

Here, $\mathbb{I}$ is the light intensity, B is the cylinder bore diameter, T_{bulk} is the in-cylinder bulk-gas temperature, p is the cylinder pressure, and k_B is the Boltzmann constant $\left(1.381 \times 10^{-23} J/K\right)$. Based on the recorded cylinder pressure, the bulk gas temperature was estimated assuming isentropic compression.

Three different datasets, namely "background", "reference", and "target", each containing 100 cycles were acquired to estimate the in-cylinder O_3. The "background" dataset accounted for the noise signal coming from the ambient light in the absence of the lamplight. The "target" and "reference" datasets were acquired with and without O_3 addition. Note that only the closed part of the cycle was considered in the O_3 measurement. During O_3 measurement, the fuel was added but the spark was kept inactive to avoid combustion in "reference" and "target" cycles. Enhanced combustion stability with O_3 addition in the "target" cycle would have led to a high amount of residual CO_2 that absorbs 266 nm light (Schulz et al. 2002). Also, the presence of combustion intermediates that absorbs UV light like hydroperoxyl (HO_2) and hydrogen peroxide (H_2O_2) (Ekoto and Foucher 2018; Kijewski and Troe 1971; Molina and Molina 1981) during LTHR and HTHR can differ in "reference" and "target" cycles. Thus, to have a correct O_3 measurement—free from absorption error by other species, combustion was suppressed by keeping the spark inactive. To compensate for the effect of combustion, the intake temperatures were increased to match the intake valve closing (IVC) temperatures of the corresponding fired cycles.

8.2.4 Single Zone Chemical Model

Chemkin-Pro 0D homogeneous reactor simulations were conducted to assess chemical kinetic pathways responsible for the fuel oxidation with O_3 addition (Ansys 2017). Several experimental parameters were matched or used during simulations to capture the relevant processes related to O_3 decomposition, radical formation, and fuel oxidation. The experimentally measured pressure and unburned gas temperature during the compression stroke were kept constrained throughout the simulation. IVC temperature and species compositions obtained from the experiments were used to initialize the simulation. O_3 oxidation chemistry from Masurier et al. (2013) added to the Lawrence Livermore National Laboratory's gasoline surrogate mechanism (Mehl et al. 2011) that yielded a total of 2028 species and 8636 reactions was used for simulations. A five-component gasoline surrogate (46.6% iso-octane, 17.8% n-heptane, 9.9% ethanol, 6.0% 1-hexene, and 19.7% toluene by liquid volume) was used to match the overall molecular composition and reactivity characteristics of RD587 gasoline (Wolk et al. 2016a).

8.3 Results and Discussion

8.3.1 Effect of O_3 on Combustion Performance and Emissions

O_3 addition enabled stable combustion relative to similar conditions without O_3 by promoting end gas reactivity. AHRR profiles are shown in Fig. 8.4 for a baseline 1000 rpm, 2.8 bar IMEP, partially stratified operating condition with and without 29 ppm of added O_3 to showcase the impact of O_3 addition on heat release characteristics. The total fueling rate was 12 mg/cycle, with ~20% of the fuel injected during the second injection. The spark timing was at −54 CA, and the second injection occurred 7 CA later. To investigate the effect of O_3 decomposition on end gas autoignition behavior, a measured O_3 profile was plotted in Fig. 8.4 for similar non-fired operating conditions. However, to capture the correct O_3 decomposition rate, the IVC temperatures between fired and non-fired cycles were closely matched.

For both conditions, the first noticeable heat release occurred around −42 CA as the stratified mixture created from the second injection was ignited. The authors speculate that this heat release is the result of a deflagration confined to the piston bowl where the second injection produced rich stratified mixtures. Until −25 CA,

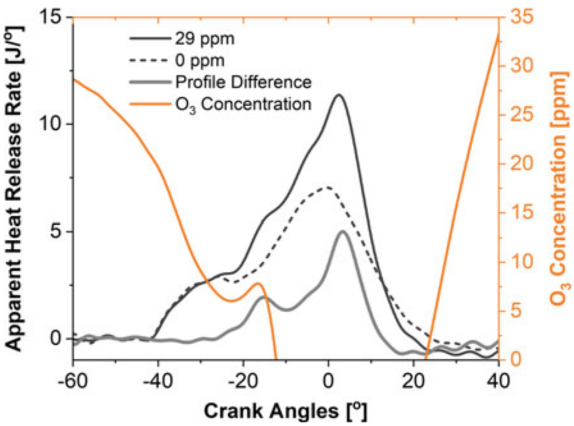

Fig. 8.4 AHRR profiles of with and without O_3 for a 1000 rpm, 2.8 bar IMEP, partially stratified operating condition

AHRR values remained closely matched for conditions with and without O_3 addition. Beyond this point, the O_3 added AHRR profile increasingly separated from the condition without O_3. The sharp increase in AHRR is not consistent with the consumption of lean end gas mixtures by deflagration alone, suggesting that additional heat release occurred because of auto-ignition of the end gas.

To illustrate more clearly the occurrence of the end gas auto-ignition, the AHRR profile for the condition without O_3 addition has been subtracted from the condition with O_3 addition and is plotted as the 'Profile Difference' in Fig. 8.4. The addition of O_3 resulted in an increase of 31% in total heat release. The profile resembles low-temperature combustion (LTC) auto-ignition, with an LTHR period starting around −25 CA and a larger high-temperature heat release (HTHR) period near TDC. The thermal decomposition of O_3 into O and O_2 began around −60 CA and almost ended with the initiation of LTHR. Secondary absorbance, which was started around −22 CA, was probably from the HO_2 formed during LTHR reactions.

Figure 8.5 plots the indicated specific fuel consumption (ISFC) and NO_x emission index (EI) for a range of engine speeds (800–1600 rpm) as a function of engine load. The O_3 concentrations were fixed at 50 ppm for homogeneous SACI and 30 ppm for partially stratified SACI. For the partially stratified SACI results, the largest declines in ISFC were observed for the lowest engine loads and speeds. Moreover, ISFC data from the homogeneous SACI had a more limited range of achievable loads and speeds similarly collapsed to the same curve. These findings show that there is no obvious punishment with stratified operation due, for instance, to a change in the features of total heat transfer.

In partially stratified SACI, NO_x emissions had a weak positive correlation with increased engine load and a much stronger positive correlation with an increased engine speed for engine speeds of 1400 rpm and lower. These trends reversed for the load sweep of the highest speed (1600 rpm) condition, which had a much stronger dependence on increased engine load. Homogeneous SACI NO_x emissions were

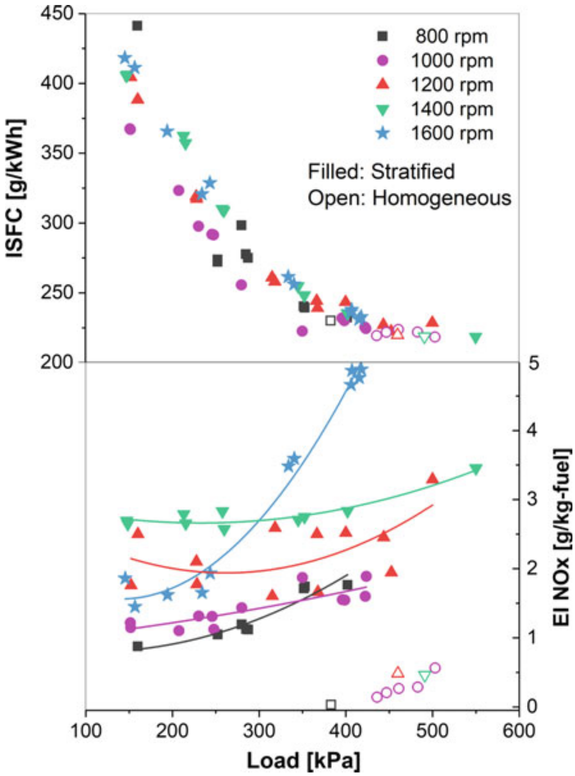

Fig. 8.5 ISFC and NO_x emissions as a function of load at engine speeds of 800–1600 rpm for O_3 seeded homogeneous versus partially stratified SACI (Biswas and Ekoto 2019b)

about an order of magnitude lower than comparable partially stratified SACI conditions, probably due to the significant reduction of high-temperature deflagration in fuel-rich stratified regions existed in the piston bowl.

Contour maps of indicated thermal efficiency (ITE), combustion efficiency, coefficient of variation (COV) of IMEP, and 50% burn angle (CA50) are plotted in Fig. 8.6 as a function of engine speed and load for partially stratified SACI. For the range of operating conditions examined, ITE values ranged from 20 to 40%. As anticipated, enhanced ITE was heavily associated with enhanced load for a specified engine speed due to a combination of greater combustion efficiency and more optimal phasing of combustion which reduced cycle-to-cycle variability. Increased ITE for a given load was also observed for a decrease in engine speeds resulting solely from higher combustion efficiency. Longer cycle durations permitted more time for lean mixture combustion to occur for the slower engine speeds.

Similar contour maps of engine-out NO_x, unburned hydrocarbon (UHC), and CO emissions are plotted in Fig. 8.7. Although the NO_x emission limit was 5 g/kg-fuel, only the highest load and speed conditions (5+ bar IMEP and 1400+ rpm) approached this limit. For higher loads and lower engine speeds, UHC and CO emissions were typically low, which is unsurprising considering that these are the regions where

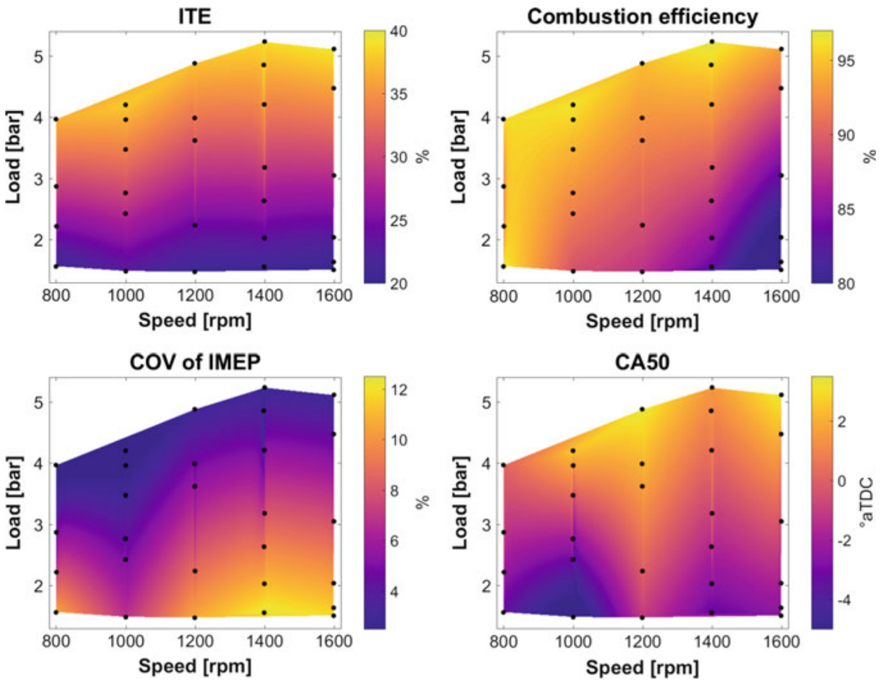

Fig. 8.6 Contour maps of ITE, combustion efficiency, CoV of IMEP, and CA50 from partially stratified SACI for a range of engine speeds (800–1600 rpm) and loads (1.5–5.5 bar IMEP)

combustion efficiency was high. As loads dropped and engine speeds increased, UHC emissions increased steadily. While CO emissions likewise increased with decreased engine load, peak values occurred at lower speeds due to a substantial conversion of hydrocarbons to CO, but the final oxidation step of CO to CO_2 being rate limited.

8.3.2 Intake Temperature and Engine Speed on O_3 Decomposition

To examine the impact of intake temperature on O_3 decomposition kinetics, measured O_3 profiles with IVC temperatures of 361 and 384 K are plotted in Fig. 8.8a alongside AHRR profiles zoomed in on the LTHR period. O_3 profiles are plotted on a semi-log scale to more clearly highlight when rapid thermal decomposition into O and O_2 occurs. Note that there was increased absorbance starting around −25 °aTDC that was not present in the reference datasets. As stated in the introduction, this increased absorbance was likely from HO_2 formed during LTHR reactions. Although the spurious absorbance was not desired, it nonetheless is a convenient marker of

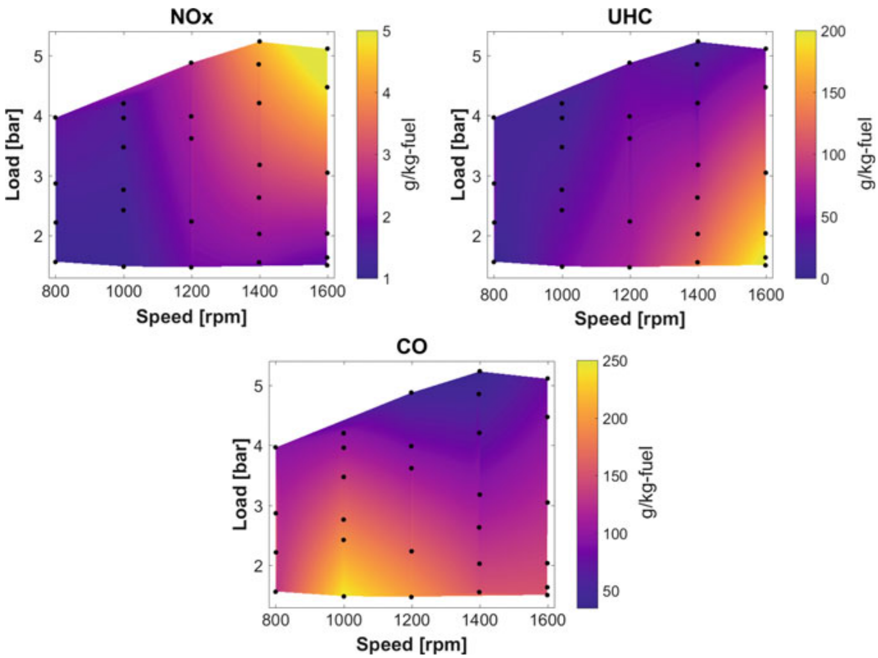

Fig. 8.7 Contour maps of engine-out NO_x, UHC, and CO emissions from partially stratified SACI for a range of engine speeds (800–1600 rpm) and loads (1.5–5.5 bar IMEP)

LTHR onset. For both profiles, rapid O_3 thermal decomposition started around −40 °aTDC, and was nearly complete by −20 °aTDC. Thermal O_3 decomposition for the higher IVC temperature condition (384 K) concluded just before the appearance of LTHR for the fired conditions with the highest intake temperature (i.e., 70 and 80 °C).

Figure 8.8b shows the in-cylinder O_3 concentration for the range of engine speeds (800–1400 rpm) along with a close-up view of LTHR period heat release rates for the fired conditions. In-cylinder O_3 concentrations gradually declined early in the cycle before the start of rapid O_3 decomposition, which occurred around −45 CA irrespective of engine speeds. Note that the only major difference for the different engine speeds was that O_3 decomposition occurred earlier in the cycle with lower engine speeds. This behavior can be attributed to the longer residence times at lower speeds that enabled a greater amount of decomposition during the cooler early portion of the cycle. Rapid thermal O_3 decomposition of O_3 ended by around −25 CA, which is about the time of LTHR onset for all fired conditions.

O_3 addition reduces the intake heating requirement and hence enables wide CA50 control for LTC. Contour plot in Fig. 8.9 shows a non-linear dependence of CA50 on intake O_3 concentration and engine temperature. The reduction in intake heating requirement is highest for smaller concentrations of O_3. The return of O_3 addition slowly diminishes with an increase in O_3 concentrations. An addition of 25 ppm of O_3

Fig. 8.8 Effect of **a** intake temperature and **b** engine speed on in-cylinder O_3 decomposition

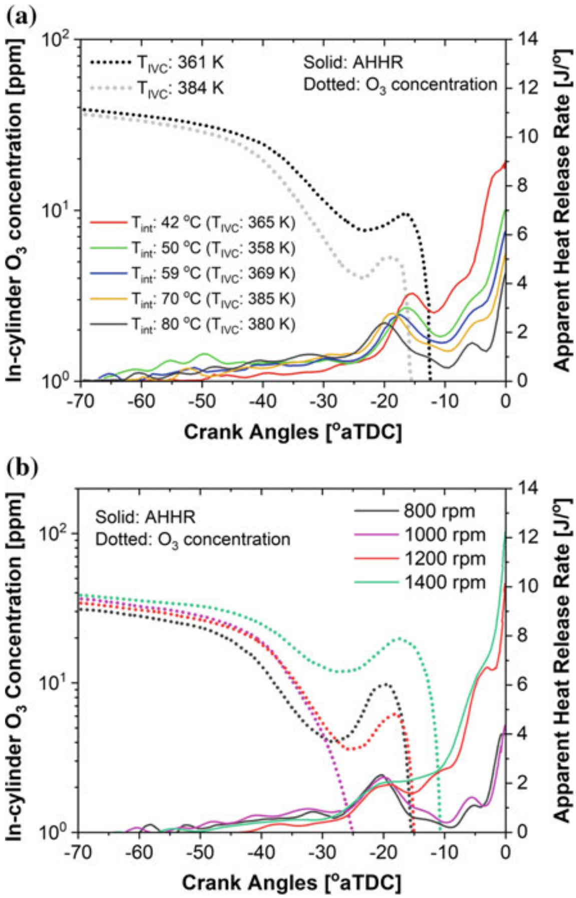

Fig. 8.9 Contour maps of CA50 as a function of intake O_3 concentration and temperature for a fixed operating point (-230 CA SOI, 1000 rpm, $\phi = 0.3$)

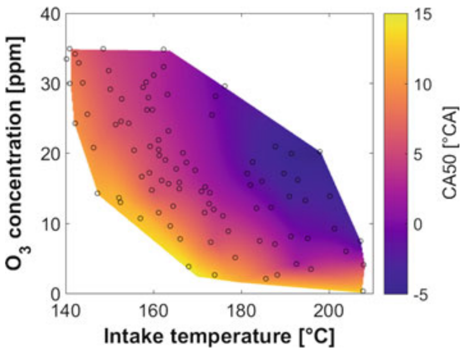

can considerably lower the intake temperature by 65 K. A lower intake temperature also implies that achieving a stable point was possible without adding O_3. Hence, O_3 provides an additional control knob to adjust the combustion phasing in ACI operation.

8.3.3 Kinetic Study of LTHR Pathway

To recognize key reaction pathways for enhanced auto-ignition chemistry with O_3 addition, 0D chemical kinetic simulations with detailed gasoline chemistry were performed. At the beginning of the simulations, experimentally estimated IVC conditions were imposed. The simulations were carried out through main compression stroke to capture relevant physics of O_3 decomposition, radical formation, and fuel oxidation. Figure 8.10 illustrates a schematic of the dominant LTHR response paths outlined in the introduction. It shows O_3 decomposed O leads to various sustainable production pathways for R and OH. Note that an additional pathway is included for completeness in which RO_2 undergoes inner isomerization to create hydroperoxyalkyl radical (QOOH).

Simulations were carried out with and without 50 ppm O_3 addition, with all other boundary conditions fixed to explore the most sensitive reactions to LTHR chemistry as illustrated in Fig. 8.10. The following engine operating condition: 1400 rpm, T_{intake} 80 °C, IMEP 4.9 bar, ST −54 °aTDC, T_{IVC} 383 K, RGF 12.5%, was chosen for this purpose. Figure 8.11 plots AHRR profiles of this operating condition along with the corresponding simulation results with and without the addition of O_3. The onset of LTHR with O_3 addition from the simulations closely matches the respective outcomes of the experiment. On the contrary, simulations without O_3 addition did not show any evidence of LTHR. Early in the cycle, O_3 concentrations are stable; however, start

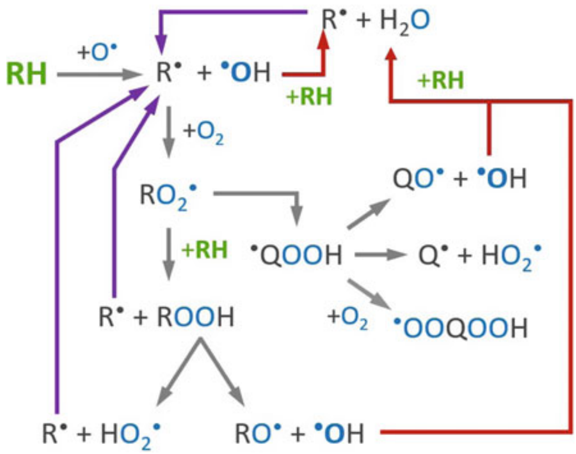

Fig. 8.10 Schematic of LTHR reaction pathways initialized by O formed from thermal decomposition of O_3. Violet and red arrows highlight the sustained source of R and OH radicals, respectively (Biswas and Ekoto 2019a)

Fig. 8.11 AHRR profiles from the engine experiment and 0D Chemkin simulations with (solid) and without (dotted) O_3 (top). Cycle evolution of O_3 and important fuel oxidation radicals highlighted in Fig. 8.10 (bottom) (Biswas and Ekoto 2019a)

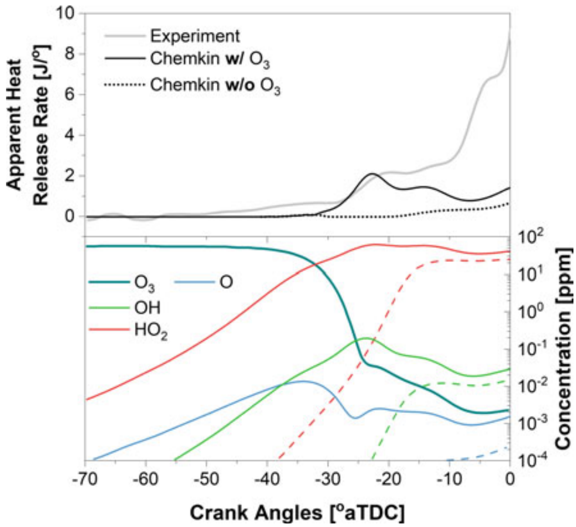

to decline rapidly at −40 °aTDC and finally reaches a negligible concentration by −25 °aTDC. These findings are well in agreement with the experimental findings shown in Fig. 8.8b. O concentrations did not exceed 0.01 ppm since it quickly consumed by fuel molecules. However, rapid decomposition of O_3 leads to the creation of O, OH, and HO_2 much sooner.

8.3.4 Energy Requirements for End Gas Auto-ignition

While end gas reactivity increased with O_3 addition, it was not sufficient on its own to lead to auto-ignition for the fuel-lean conditions examined in this study. Additional thermal energy supplied by the fuel-rich bowl deflagration was needed to accelerate end gas auto-ignition reactions. However, results from the previous section demonstrated that the second injection was the primary source of NO_x emissions. Thus, it is imperative to minimize the second injection fueling fraction while preserving good combustion stability and efficiency for a given condition, which requires new design tools. In this section, a simplified analysis is presented to evaluate the end gas thermal energy deficit needed to initiate sufficiently strong auto-ignition. Optimized conditions used to generate performance and emissions maps in Figs. 8.6 and 8.7 were used as the reference points.

It was observed earlier that heat release rates from the initial bowl deflagration were well-matched, regardless of the amount of in-cylinder O_3 concentration. Accordingly, the increased thermal energy from the early deflagration can be estimated from the integrated heat release up to the onset of LTHR. The beginning of LTHR for each condition was identified from the 'profile difference' between the

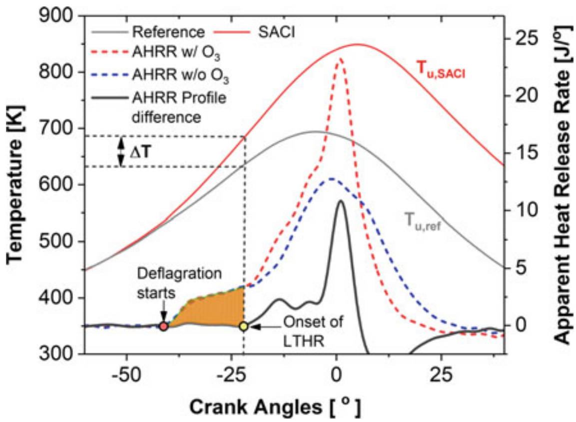

Fig. 8.12 Schematic used to illustrate the methods used to estimate energy requirement for end gas auto-ignition

same operating conditions with and without O_3 addition as illustrated in Fig. 8.12. The orange hatched area represents the integrated energy that is attributed exclusively to the early deflagration heat release.

While the integrated heat release provides an estimate for thermal energy addition, it is not very predictive. An alternate method that is potentially more predictive is to evaluate the auto-ignition energy using cycle thermodynamic parameters. For this method, a simple two-zone system was assumed, with deflagration in the piston bowl growing outwardly and end gas mixture getting compressed by this deflagration, as shown in Fig. 8.2. Deflagration and end gas zones were assumed to be quasi-steady and homogenous, with each zone identified by a single burned or unburned temperature. Thus, the energy required for auto-ignition was the difference in unburned end gas enthalpies for an operating condition relative to a reference motored condition without deflagration. The estimated energy deficit required to initiate end gas auto-ignition can then be written as,

$$E = m_u C_{p,u}\left(T_{u,SACI} - T_{u,ref}\right) \tag{8.2}$$

where m_u is the end gas mass of, $C_{p,u}$ is the end gas constant pressure specific heat, $T_{u,SACI}$ is unburned end gas temperature for stratified SACI condition, i.e., with O_3 seeding and the presence of deflagration providing additional energy, and $T_{u,ref}$ is the reference temperature from a corresponding motored condition.

A map of the calculated thermal energy deficit (integrated heat release up to LTHR onset) required for end gas auto-ignition is plotted in Fig. 8.13a for the full range of load and engine speed conditions evaluated in the present study. The energy deficit varied from 10 J for highest load and lowest speed conditions (4 bar IMEP, 800 rpm) to 40 J for the lowest loads and highest engine speed conditions (1.5 bar IMEP, 1600 rpm). These results are unsurprising given the longer residence times and more reactive mixtures for the highest load and lowest speed conditions. Indeed, it was often observed that these conditions could sustain auto-ignition without a spark,

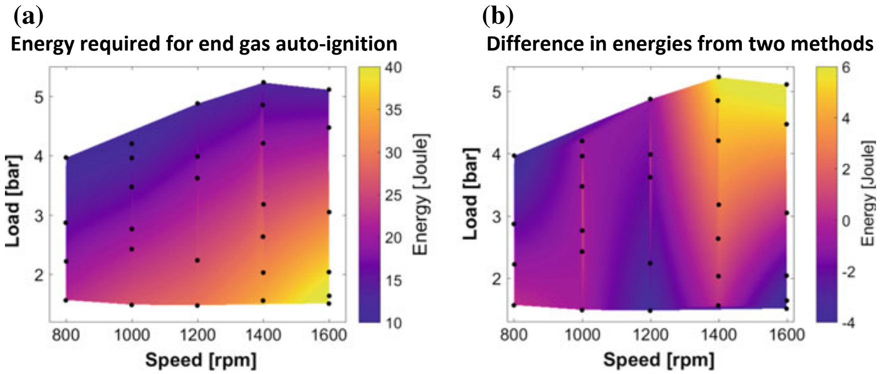

Fig. 8.13 End gas auto-ignition energy **a** estimated from the integrated heat release up to LTHR onset, **b** difference estimated from two methods, i.e. energy integrated heat release (method 1) and Eq. (8.2) (method 2)

utilizing only energy addition from retained residual heating. The maps illustrate a fairly linear transition between these two extreme regions.

A map illustrating the difference in thermal energies estimated by integrated heat release (method 1) and from Eq. (8.2) (method 2) is plotted in Fig. 8.13b. It is immediately apparent that energy trends for both methods are remarkably well matched. The largest differences between the two methods were observed for the highest load conditions. Relative to the end gas thermal energy deficit calculation that used the integrated heat release, the method that used the difference in end gas temperatures at the onset of LTHR predicts modestly higher values for the lowest engine speeds (0–4 J) and modestly lower values (0–6 J) for the highest speeds. Potential reasons for the discrepancy include: (a) errors in the estimated temperature calculation at LTHR onset, (b) end gas thermal stratification that would have led to reduced thermal energy requirements for local hot spots, and (c) potential fuel stratification from the second injection that likewise would have led locally rich regions that ignite earlier. Future work will evaluate each of these sensitivity parameters in greater detail.

8.3.5 Development of Advanced Ignition System

O_3 added homogeneous SACI failed to operate at lower loads compared to stratified SACI which enabled stable combustion across the entire load speed map. However, partially stratified SACI operation was responsible for a 3–5 folds increase in NO_x emissions. Thus, an optimum combustion strategy is crucial to enable stable combustion with lesser emission. The advanced ignition system has the potential to bridge these two requirements—stable combustion with lower emissions.

Transient Plasma Ignition (TPI) is a promising advanced ignition technology that utilizes short pulse (~10 s of nanoseconds), high-voltage (15 kV+) electrical discharges to generate highly energized low-temperature plasma (LTP). Our preliminary study (Biswas et al. 2018) shows that TPI extends the lean limit and increase the dilution tolerance of propane/air mixture compared to conventional inductive spark. TPI promotes faster flame propagation rates through a combination of larger volume ignition kernels and the generation of active radicals that enhance flame speeds. Visualization of ignition event and early flame propagation by transient plasma was performed within a custom-built optically accessible spark calorimeter for near-atmospheric, 1.3 bar, $\phi = 0.41$–1.0 propane/air mixtures. A barrier discharge igniter (BDI) with an anode tip covered by high-temperature, high-dielectric strength epoxy was used for TPI.

Figure 8.14 compares the pressure and heat release rate of TPI with an inductive spark. Figure 8.14a shows that for $\phi = 0.6$ the ignition delay was shorter for TPI. Also, a steeper slope in TPI pressure profile indicates that combustion by transient plasma happens faster than an inductive spark. To compare the performance of lean TPI, pressure history of stoichiometric spark ignition is also plotted in Fig. 8.14a. The pressure rise rate is nearly identical for TPI $\phi = 0.6$ to stoichiometric spark ignition. This indicates that plasma ignition produces stronger ignition kernels and faster flame propagation even at the leaner operating condition. This is also evident from the heat release rate (HRR) profiles shown in Fig. 8.14b. At $\phi = 0.6$, the peak heat release rate doubled for TPI compared to inductive spark. TPI had a burn duration of 10 ms, compared to a burn duration of 23 ms for inductive spark. This shows that the flame growth rate in TPI is much faster compared to spark ignition for $\phi = 0.6$. The HRR at $\phi = 0.6$ for TPI matched closely with stoichiometric HRR from spark ignition.

Transient plasma discharges lead to increased ionization and dissociation. Previous studies (Wolk et al. 2013; Cathey et al. 2008) have shown that TPI generates radicals and other electronically excited species over a relatively large volume. Plasma discharges dissociate O_2 to create O which again combines with O_2 to produce O_3. We measured LTP generated O_3 in desiccated air at different pressure and voltage

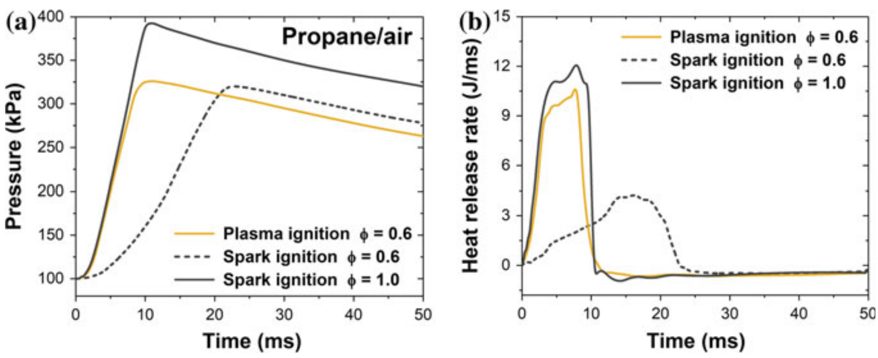

Fig. 8.14 **a** Pressure history and **b** heat release rate from low-temperature plasma and inductive spark ignition in stoichiometric and $\phi = 0.6$ propane/air

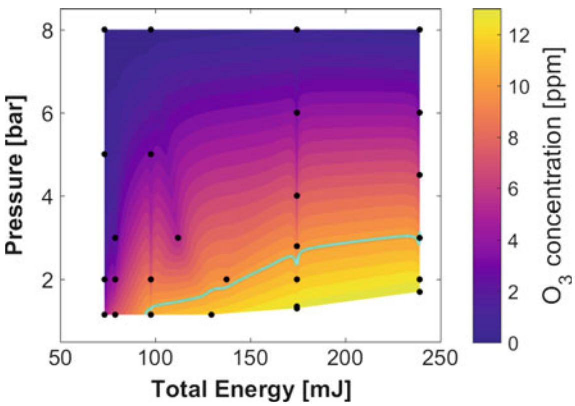

Fig. 8.15 The contour plot of O_3 generated by low-temperature plasma discharges (10 pulses) in desiccated air at engine condition. The cyan line represents an O_3 concentration of 10 ppm

conditions in a 29 cc optically accessible spark calorimeter. Then the estimated O_3 concentrations were converted to engine conditions of 0.55 L volume and 1 bar intake pressure. The contour map of generated O_3 at the engine condition is shown in Fig. 8.15. The cyan line represents 10 ppm of O_3. Note that these 10 ppm O_3 was generated by a discharge of 10 pulses with the time difference between each pulse was 100 microseconds. Thus, to reach an O_3 concentration of 50 ppm, 5 such discharges will be necessary. However, the rate of O_3 generation decreases at higher pressure. Sine in-cylinder pressure changes in non-linear fashion during the compression stroke, an optimum pulsing strategy need to be utilized to achieve the target amount of O_3 necessary for end gas auto-ignition.

8.4 Summary

In the present study, performance and emissions characteristics were investigated for 0–50 ppm O_3 added lean SACI operation with two different injection strategies, (1) partially stratified: double injection—early (75–90% fuel) and late DI (10–25% fuel) and (2) homogeneous: single early direct injection (DI) in an optically accessible single-cylinder research engine. Significant findings are as follows:

- O_3 addition stabilized engine combustion relative to comparable conditions without O_3 by increasing end gas reactivity. Increased intake O_3 addition—and hence late-cycle O—led to a corresponding increase in end gas LTHR that accelerated the onset of HTHR.
- The addition of O_3 was most useful for the lowest engine speeds due to the longer cycle residence times for kinetically controlled heat release to occur. The impact of O_3 addition decreased with increased engine speed due to shorter residence times available for auto-ignition.

- Increased fueling fractions in the late second injection likewise increased the strength of the early deflagration, which generally increased combustion stability but led to rapid increases in NO_x emissions.
- Lower loads were more challenging to achieve in O_3 enhanced homogeneous SACI relative to partially stratified SACI. However, homogeneous SACI approach generated higher efficiencies and lesser emissions.
- A simplified thermodynamic analysis method was developed to calculate the energy deficit that used either the integrated heat release up to the onset of LTHR or the difference in the end gas temperatures for cycles with and without combustion. Both methods exhibited excellent agreement with each other. For the conditions examined here, roughly 10–40 J of thermal energy was needed from the early deflagration to lead to optimized end gas autoignition. Higher speed and lower load conditions required the most energy due to the shorter residence times and leaner end gas mixtures.

The present study demonstrates that the best way to dramatically reduce NO_x emissions is to eliminate the late second injection altogether. O_3 addition helps with this by increasing the strength of end gas LTHR reactions and thus requiring a weaker bowl deflagration. While further reductions of second injection fueling fraction are likely possible with even higher O_3 concentrations, this is like not sufficient to entirely eliminate the second injection. It would be desirable to have a strong deflagration without the second injection, which highlights how the current strategy could be augmented by some form of the advanced ignition system (e.g., pre-chamber, low-temperature plasma).

Acknowledgements The authors would like to thank Alberto Garcia, Gary Hubbard, and Keith Penney for their dedicated support of the Gasoline Combustion Fundamentals Laboratory. The work was performed at the Combustion Research Facility, Sandia National Laboratories, Livermore, CA. Financial support was provided by the U.S. Department of Energy, Vehicle Technologies Office. Sandia National Laboratories is a multi-mission laboratory managed and operated by National Technology and Engineering Solutions of Sandia, LLC., a wholly-owned subsidiary of Honeywell International, Inc., for the U.S. Department of Energy's National Nuclear Security Administration under contract DE-NA0003525.

References

Ansys (2017) CHEMKIN-PRO

Benajes J, García A, Domenech V, Durrett R (2013) An investigation of partially premixed compression ignition combustion using gasoline and spark assistance. Appl Therm Eng 52(2):468–477

Benajes J, Molina S, García A, Monsalve-Serrano J, Durrett R (2014) Performance and engine-out emissions evaluation of the double injection strategy applied to the gasoline partially premixed compression ignition spark assisted combustion concept. Appl Energy 134:90–101

Biswas S (2018) Physics of turbulent jet ignition: mechanisms and dynamics of ultra-lean combustion, 1st edn. Springer

Biswas S, Ekoto I (2019a) Detailed investigation into the effect of ozone addition on spark assisted compression ignition engine performance and emissions characteristics. SAE Technical Paper 2019-01-0966

Biswas S, Ekoto I (2019b) Spark assisted compression ignition engine with stratified charge combustion and ozone addition. JSAE 20199089

Biswas S, Qiao L (2016) Prechamber hot jet ignition of ultra-lean H_2/air mixtures: effect of supersonic jets and combustion instability. SAE Int J Engines 9(3)

Biswas S, Tanvir S, Wang H, Qiao L (2016) On ignition mechanisms of premixed CH_4/air and H_2/air using a hot turbulent jet generated by pre-chamber combustion. Appl Therm Eng 106:925–937

Biswas S, Ekoto I, Scarcelli R (2018) Transient plasma ignition (TPI) for automotive applications. In: 4th international conference on ignition systems for gasoline engines. Berlin

Cathey C, Cain J, Wang H, Gundersen MA (2008) OH production by transient plasma and mechanism of flame ignition and propagation in quiescent methane-air mixtures. Combust Flame 154(4)

Chang J, Güralp O, Filipi Z, Assanis D, Kuo T-W, Najt P, Rask R (2004) New heat transfer correlation for an HCCI engine derived from measurements of instantaneous surface heat flux. SAE Technical Paper 2004-01-2996

Christensen M, Johansson B, Einewall P (1997) Homogeneous charge compression ignition (HCCI) using isooctane, ethanol and natural gas—a comparison with spark ignition operation. SAE Technical Paper 972874 106(4)

Dec JE (2009) Advanced compression-ignition engines—understanding the in-cylinder processes. Proc Combust Inst 32(2):2727–2742

Dec JE, Yang Y, Dernotte J, Ji C (2015) Effects of gasoline reactivity and ethanol content on boosted, premixed and partially stratified low-temperature gasoline combustion (LTGC). SAE Int J Engines 8(3)

Depcik C, Mangus M, Ragone C (2014) Ozone-assisted combustion—part I: literature review and kinetic study using detailed n-heptane kinetic mechanism. J Eng Gas Turb Power 136(9)

Dernotte J, Dec JE, Ji C (2015) Energy distribution analysis in boosted HCCI-like/LTGC engines—understanding the trade-offs to maximize the thermal efficiency. SAE Int J Engines 8(3)

Ekoto I, Foucher F (2018) Mechanisms of enhanced reactivity with ozone addition for advanced compression ignition. In: SAE world congress experience. SAE International, Detroit, MI

Ekoto I, Wolk B, Northrop W (2017) Energy analysis of low-load low-temperature gasoline combustion with auxiliary-fueled negative valve overlap. SAE Int J Engines 10(3):1238–1255

Fitzgerald RP, Steeper R (2010) Thermal and chemical effects of NVO fuel injection on HCCI combustion. SAE Int J Engines 3(1):46–64

Gorshelev V, Serdyuchenko A, Weber M, Chehade W, Burrows JP (2014) High spectral resolution ozone absorption cross-sections—part 1: measurements, data analysis and comparison with previous measurements around 293 K. Atmos Meas Tech 7(2):609–624

Graham LA, Belisle SL, Rieger P (2009) Nitrous oxide emissions from light duty vehicles. Atmos Environ 43(12):2031–2044

Kijewski H, Troe J (1971) Study of the pyrolysis of H_2O_2 in the presence of H_2 and CO by use of UV absorption of HO_2. Int J Chem Kinet 3(3):223–235

Kolodziej C, Kodavasal J, Ciatti S, Som S, Shidore N, Delhom J (2015) Achieving stable engine operation of gasoline compression ignition using 87 AKI gasoline down to idle. SAE Technical Paper 2015-01-0832

Lavoie GA, Martz J, Wooldridge M, Assanis D (2010) A multi-mode combustion diagram for spark assisted compression ignition. Combust Flame 157(6):1106–1110

Lawler BJ, Filipi ZS (2013) Integration of a dual-mode SI-HCCI engine into various vehicle architectures. J Eng Gas Turb Power Trans ASME 135(5)

Manofsky L, Vavra J, Assanis DN, Babajimopoulos A (2011) Bridging the gap between HCCI and SI: spark-assisted compression ignition. SAE Int

Masurier JB, Foucher F, Dayma G, Dagaut P (2013) Homogeneous charge compression ignition combustion of primary reference fuels influenced by ozone addition. Energy Fuels 27(9):5495–5505

Masurier JB, Foucher F, Dayma G, Dagaut P (2015a) Ozone applied to the homogeneous charge compression ignition engine to control alcohol fuels combustion. Appl Energy 160(Supplement C):566–580

Masurier J-B, Foucher F, Dayma G, Dagaut P (2015b) Investigation of iso-octane combustion in a homogeneous charge compression ignition engine seeded by ozone, nitric oxide and nitrogen dioxide. Proc Combust Inst 35(3):3125–3132

Mehl M, Pitz WJ, Westbrook CK, Curran HJ (2011) Kinetic modeling of gasoline surrogate components and mixtures under engine conditions. Proc Combust Inst 33:193–200

Middleton RJ, Olesky LKM, Lavoie GA, Wooldridge MS, Assanis DN, Martz JB (2015) The effect of spark timing and negative valve overlap on spark assisted compression ignition combustion heat release rate. Proc Combust Inst 35(3):3117–3124

Molina LT, Molina MJ (1981) UV absorption cross-sections of HO_2NO_2 vapor. J Photochem 15(2):97–108

Olesky LM, Martz JB, Lavoie GA, Vavra J, Assanis DN, Babajimopoulos A (2013) The effects of spark timing, unburned gas temperature, and negative valve overlap on the rates of stoichiometric spark assisted compression ignition combustion. Appl Energy 105:407–417

Olesky LM, Lavoie GA, Assanis DN, Wooldridge MS, Martz JB (2014) The effects of diluent composition on the rates of HCCI and spark assisted compression ignition combustion. Appl Energy 124:186–198

Olesky LKM, Middleton RJ, Lavoie GA, Wooldridge MS, Martz JB (2015) On the sensitivity of low temperature combustion to spark assist near flame limit conditions. Fuel 158:11–22

Ombrello T, Won SH, Ju YG, Williams S (2010) Flame propagation enhancement by plasma excitation of oxygen. Part I: effects of O_3. Combust Flame 157(10):1906–1915

Ortiz-Soto EA, Lavoie GA, Martz JB, Wooldridge MS, Assanis DN (2014) Enhanced heat release analysis for advanced multi-mode combustion engine experiments. Appl Energy 136:465–479

Persson H, Hultqvist A, Johansson B, Remón A (2007) Investigation of the early flame development in spark assisted HCCI combustion using high speed chemiluminescence imaging. SAE Int

Pinazzi PM, Foucher F (2017) Potential of ozone to enable low load operations of a gasoline compression ignition (GCI) engine. In: SAE world congress experience. SAE International, Detroit, MI

Reuss DL, Kuo T-W, Silvas G, Natarajan V, Sick V (2008) Experimental metrics for identifying origins of combustion variability during spark-assisted compression ignition. Int J Engine Res 9(5):409–434

Rousso AC, Hansen N, Jasper AW, Ju Y (2018) Low-temperature oxidation of ethylene by ozone in a jet-stirred reactor. J Phys Chem 122:8674–8685

Saxena S, Bedoya ID (2013) Fundamental phenomena affecting low temperature combustion and HCCI engines, high load limits and strategies for extending these limits. Prog Energy Combust Sci 39(5)

Schulz C, Koch JD, Davidson DF, Jeffries JB, Hanson RK (2002) Ultraviolet absorption spectra of shock-heated carbon dioxide and water between 900 and 3050 K. Chem Phys Lett 355(1–2):82–88

Smekhov GD, Ibraguimova LB, Karkach SP, Skrebkov OV, Shatalov OP (2007) Numerical simulation of ignition of a hydrogen-oxygen mixture in view of electronically excited components. High Temp 45(3):395–407

Srivastava DK, Weinrotter M, Kofler H, Agarwal AK, Wintner E (2009) Laser-assisted homogeneous charge ignition in a constant volume combustion chamber. Opt Lasers Eng 47:680–685

Stanglmaier RH, Roberts CE (1999) Homogeneous charge compression ignition (HCCI): benefits, compromises, and future engine applications. SAE Int J Engines 108(3):2138–2145

Stone R (1999) Compression ignition engines. In: Introduction to internal combustion engines. Springer, Palgrave, London

Truedsson I, Rousselle C, Foucher F (2017) Ozone seeding effect on the ignition event in HCCI combustion of gasoline-ethanol blends. In: SAE world congress experience. SAE Technical Paper 2017-01-0727. SAE International, Detroit, MI

Uddi M, Jiang NB, Mintusov E, Adamovich IK, Lempert WR (2009) Atomic oxygen measurements in air and air/fuel nanosecond pulse discharges by two photon laser induced fluorescence. Proc Combust Inst 32:929–936

United States Environmental Protection Agency, Office of Policy and Evaluation (2016) Inventory of U.S. greenhouse gas emissions and sinks: 1990–2014. U.S. Environmental Protection Agency, Washington, DC

United States, Environmental Protection Agency, Office of Transportation and Air Quality (2012) Non-conformance penalties for heavy-duty diesel engines subject to the 2010 NO_x emission standard. U.S. Environmental Protection Agency, Office of Transportation and Air Quality, Washington, DC

Weinrotter M, Wintner E, Iskra K, Neger T, Olofsson J, Seyfried H, Aldén M, Lackner M, Winter F, Vressner A, Hultqvist A, Johansson B (2005) Optical diagnostics of laser-induced and spark plug assisted HCCI combustion. SAE Technical Paper 2005-01-0129

Wolk B, DeFilippo A, Chen JY, Dibble R, Nishiyama A, Ikeda Y (2013) Enhancement of flame development by microwave-assisted spark ignition in constant volume combustion chamber. Combust Flame 160(7):1225–1235

Wolk B, Ekoto I, Northrop W (2016a) Investigation of fuel effects in negative valve overlap reforming chemistry using gas chromatography. SAE Int J Engines 9(2)

Wolk B, Ekoto I, Northrop WF, Moshammer K, Hansen N (2016b) Detailed speciation and reactivity characterization of fuel-specific in-cylinder reforming products and the associated impact on engine performance. Fuel 185:348–361

Zádor J, Taatjes CA, Fernandes RX (2011) Kinetics of elementary reactions in low-temperature autoignition chemistry. Prog Energy Combust Sci 37(4):371–421

Zhang Y, Zhu M, Zhang Z, Shang R, Zhang D (2016) Ozone effect on the flammability limit and near-limit combustion of syngas/air flames with N_2, CO_2, and H_2O dilutions. Fuel 186(Supplement C):414–421

Zhao F, Asmus TN, Assanis DN, Dec JE, Eng JA, Najt PM (2003) Homogeneous charge compression ignition (HCCI) engines: key research and development issues. Society of Automotive Engineers International, Warrendale, PA